

Universal dynamics in an isolated one-dimensional Bose gas far from equilibrium

Sebastian Erne^{1,2,3}, Robert Bücke^{1,4}, Thomas Gasenzer^{2,5}, Jürgen Berges² & Jörg Schmiedmayer^{1*}

Understanding the behaviour of isolated quantum systems far from equilibrium and their equilibration is one of the most pressing problems in quantum many-body physics^{1,2}. There is strong theoretical evidence that sufficiently far from equilibrium a wide variety of systems—including the early Universe after inflation^{3–6}, quark–gluon matter generated in heavy-ion collisions^{7–9}, and cold quantum gases^{4,10–14}—exhibit universal scaling in time and space during their evolution, independent of their initial state or microscale properties. However, direct experimental evidence is lacking. Here we demonstrate universal scaling in the time-evolving momentum distribution of an isolated, far-from-equilibrium, one-dimensional Bose gas, which emerges from a three-dimensional ultracold Bose gas by means of a strong cooling quench. Within the scaling regime, the time evolution of the system at low momenta is described by a time-independent, universal function and a single scaling exponent. The non-equilibrium scaling describes the transport of an emergent conserved quantity towards low momenta, which eventually leads to the build-up of a quasi-condensate. Our results establish universal scaling dynamics in an isolated quantum many-body system, which is a crucial step towards characterizing time evolution far from equilibrium in terms of universality classes. Universality would open the possibility of using, for example, cold-atom set-ups at the lowest energies to simulate important aspects of the dynamics of currently inaccessible systems at the highest energies, such as those encountered in the inflationary early Universe.

Relaxation and thermalization generally result in loss of information about the details of the initial state of the system. However, the unitary quantum evolution of isolated systems preempts any such loss on a fundamental level. One way to resolve this contradiction reasons that the complexity of the many-body states involved and their dynamics lead to an insensitivity to the initial state for any realistic observable^{1,2}. Consequently, at late times, the system can be characterized by only a few conserved quantities.

Another path to loss of details about the underlying, microscale physics is through universality, such as critical scaling of correlations near phase transitions¹⁵. Aspects of universality in non-equilibrium systems have been discussed in many contexts, such as turbulence¹⁶, driven dissipative systems^{17,18}, defect formation when crossing a phase transitions^{19–21}, and the phenomenon of coarsening²² and ageing²³. Little is known about whether and how unitary time evolution from a general far-from-equilibrium state is connected to universality.

It has recently been proposed that isolated systems far from equilibrium can exhibit universal scaling in time and space associated with non-thermal fixed points^{3,4,7,10}. There is growing theoretical evidence for non-thermal universality classes, even away from any phase transition, that encompass relativistic and non-relativistic systems^{4,7}. In contrast to equilibrium critical phenomena, these non-equilibrium attractor solutions do not require any fine tuning of parameters. Moreover, the non-thermal scaling solutions do not

describe a time-translation-invariant state, whereas, for example, the scaling around a thermalized¹⁵ or pre-thermalized state does^{24–26}.

Here we study the dynamics of a repulsively interacting Bose gas after a strong cooling quench and identify a time window during which the system exhibits universal behaviour far from equilibrium. We start our experiment with a thermal gas of ultracold ⁸⁷Rb atoms in an extremely elongated, quasi-one-dimensional (in the z direction) harmonic trap (transverse confinement $\omega_{\perp} = 2 \times 10^4 \text{ s}^{-1}$, longitudinal confinement $\omega_{\parallel} = 30 \text{ s}^{-1}$) just above the critical temperature. In the final cooling step, the trap depth is lowered rapidly compared to the longitudinal thermalization timescale (Fig. 1a). This leads to fast removal of high-energy atoms, predominantly in the radially excited states, and hence constitutes an almost instantaneous cooling quench of the system. At the end of the cooling ramp, the trap depth lies below the first radially excited energy level and only longitudinal excitations remain. After a short holding period of 1 ms, which allows the atoms with large transverse energies to leave, we rapidly increase the trap depth. In this way, we prepare an isolated, far-from-equilibrium, one-dimensional system. The gas is then left to evolve in the deep potential for variable times t up to about 1 s, during which time the universal scaling dynamics takes place.

We probe the evolution of the system through two sets of measurements (see Methods for details). First, the in situ density $\rho(z, t)$ is measured using standard absorption imaging²⁷ after a short time of flight of $t_{\text{tof}} = 1.5$ ms, during which the expansion is predominantly along the tightly confined radial direction. Second, the momentum distribution $n(k, t)$ of the trapped gas is measured after a long time of flight of $t_{\text{tof}} = 46$ ms using single-atom-resolved fluorescent imaging in a thin light sheet²⁸. For each hold time t , the distributions are averaged over many independent measurements (Methods).

A typical time evolution of each of these profiles is shown in Fig. 1b. The far-from-equilibrium state at early times exhibits strongly broadened density and momentum distributions. At early times, the momentum distribution $n(k)$ follows a characteristic exponential decay, $n(k) \propto \exp(-k\xi_s)$, for large k . At late times, the system relaxes to thermal equilibrium and is well described by a thermal quasi-condensate (Fig. 1c, Extended Data Fig. 1; see Methods for details). The momentum distribution is then described by only a Lorentzian function, with width given by the thermal coherence length $\lambda_T = 2\hbar^2\rho(z)/(mk_B T)$, where \hbar is the reduced Planck constant, m is the mass of the atoms, k_B is the Boltzmann constant and T is the temperature. During the evolution, a clear peak emerges at low momenta, signalling the quasi-condensation of the system in momentum space. In the following, we analyse the thermalization process, providing a link between the far-from-equilibrium state at early times and the final equilibrium state that is observed.

For the initial state of the far-from-equilibrium evolution, we find $n(k)$ in good agreement with a theoretical model of randomly distributed solitonic defects¹² (RDM; Fig. 1c). At low momenta, the RDM has a Lorentzian shape, $n(k) \propto [1 + (k/n_s)^2]^{-1}$, with width defined by the defect density n_s . At high momenta, $n(k)$ exhibits characteristic

¹Vienna Center for Quantum Science and Technology, Atominstiut, TU Wien, Vienna, Austria. ²Institut für Theoretische Physik, Ruprecht-Karls-Universität Heidelberg, Heidelberg, Germany.

³School of Mathematical Sciences, Centre for the Mathematics and Theoretical Physics of Quantum Non-Equilibrium Systems, University of Nottingham, Nottingham, UK. ⁴Max Planck Institute for the Structure and Dynamics of Matter, Hamburg, Germany. ⁵Kirchhoff-Institut für Physik, Ruprecht-Karls-Universität Heidelberg, Heidelberg, Germany. *e-mail: schmiedmayer@atomchip.org

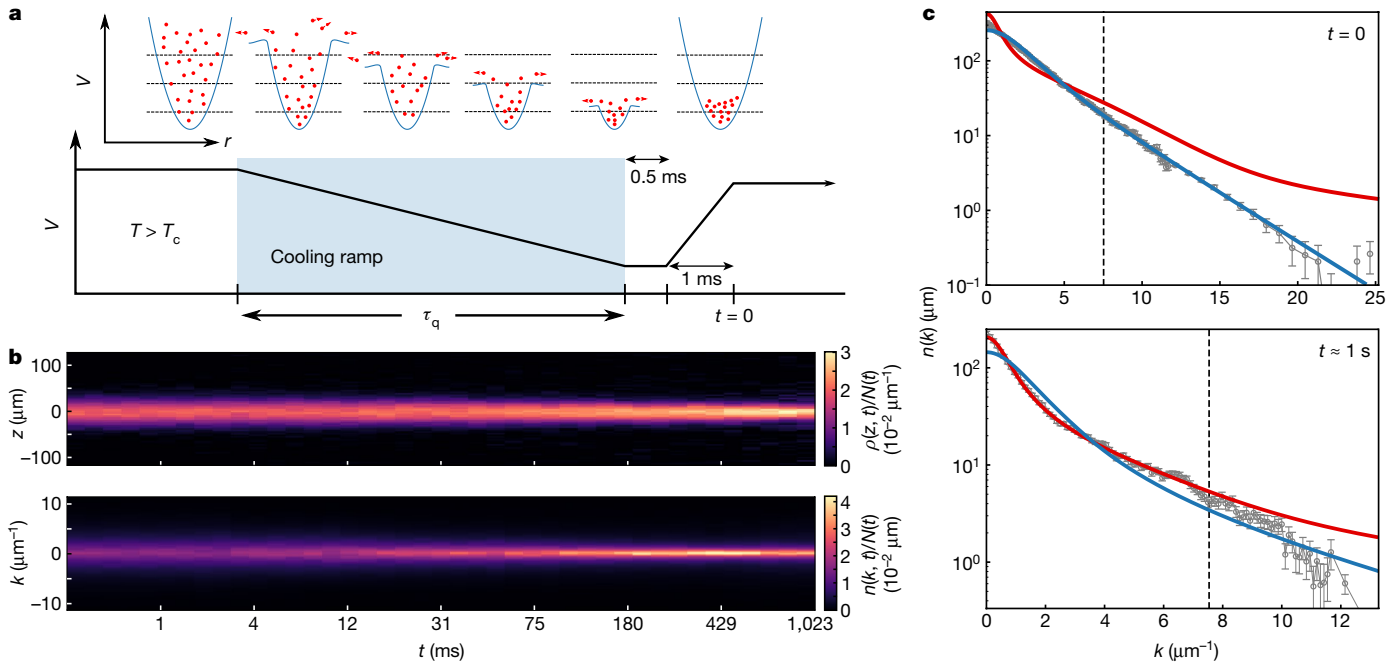


Fig. 1 | Cooling quench and late-time evolution. **a**, Schematic of the experimental cooling quench. During the quench (blue-shaded region), the trap depth V in the radial direction r (upper panel) is ramped linearly to its final value within a time $\tau_q \approx 7$ ms by applying radio-frequency radiation at a time-dependent frequency (radio-frequency knife; lower panel). The final value of V is below the first radially excited state (indicated by the dashed lines), which allows atoms (red dots) at higher energies to leave the trap (red arrows). The trap depth is held at its final position for approximately 0.5 ms to allow the hot atoms to leave and then raised within 1 ms to close the trap (see Methods). The resulting isolated, far-from-equilibrium, one-dimensional Bose gas is then measured after

a variable time t . **b**, Time evolution of the density $\rho(z, t)$ (upper panel; colour scale) and of the single-particle momentum distribution $n(k, t)$ (lower panel). Each distribution is normalized to the time-dependent atom number $N(t)$. **c**, Initial (upper panel) and final (lower panel) momentum distributions $n(k)$. The data for high momenta are binned over seven adjacent k values to lower the noise level. Error bars mark the standard error of the mean. The solid blue and red lines are theoretical fits using the random-soliton model and a thermal quasi-condensate, respectively (Extended Data Fig. 1). The vertical dashed lines correspond to the momenta of the first radially excited state.

exponential decay, $n(k) \propto \exp(-k\xi_s)$, determined by the width ξ_s of the localized density suppression associated with a solitonic defect.

Because we probe the system immediately after the almost instantaneous quench, these defects are not equilibrated (Extended Data Fig. 1); they have a reduced defect width of $\xi_s = 0.07 \mu\text{m} \approx \xi_h/3$ and a very high density of $n_s = 1.4 \mu\text{m}^{-1}$. The peak healing length $\xi_h = \hbar / \sqrt{2mg_{1D}n_0}$ determines the equilibrium width of a soliton, where $g_{1D} = 2\hbar a_s \omega_{\perp}$ is the one-dimensional interaction constant, a_s is the s -wave scattering length of ^{87}Rb and n_0 is the peak density. Although the nucleation of

solitons is predicted by the Kibble–Zurek mechanism¹⁹, the almost instantaneous quench creates an initial state with a strong overpopulation of high-energy modes. This very far-from-equilibrium state sets the initial conditions for the subsequent thermalization process and facilitates the observation of the emerging universal dynamics during the relaxation of the system.

The time evolution of the normalized momentum distribution $n(k, t)/N(t)$, where $N(t)$ is the total atom number at time t , is shown in Fig. 2a for the first 75 ms following the quench. The distribution

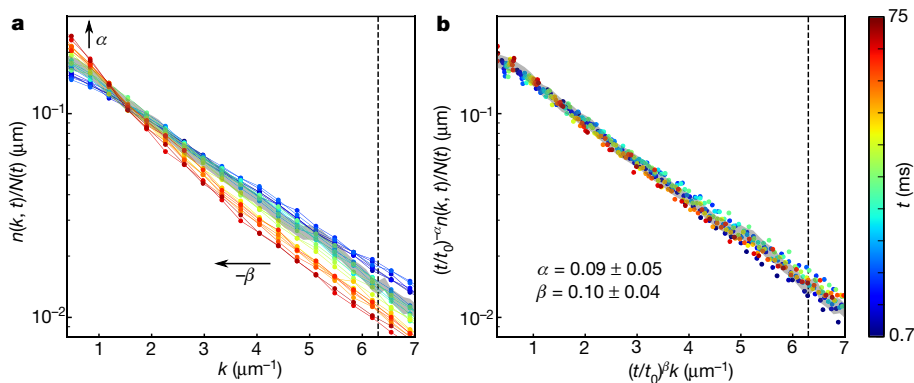


Fig. 2 | Universal scaling dynamics. **a**, Time evolution of the momentum distribution. For better visibility, the data are binned over three adjacent points in momentum space, with the time encoded by the colour scale. The grey line indicates the reference distribution at $t_0 = 4.7$ ms; its width depicts the 95% confidence interval at t_0 . The vertical dashed line marks the high-momentum cut-off for the scaling region. The arrows indicate the

scaling of the distribution in time according to equation (1). **b**, Momentum distribution rescaled according to equation (1). When depicted as a rescaled function $(t/t_0)^{-\alpha} n(\tilde{k}, t)$ of the rescaled variables $\tilde{k} = (t/t_0)^{\beta} k$, the data for all times collapse to a single curve, representing the distribution at the reference time t_0 . The exponents $\alpha = 0.09 \pm 0.05$ and $\beta = 0.10 \pm 0.04$ are determined from the maximum-likelihood function.

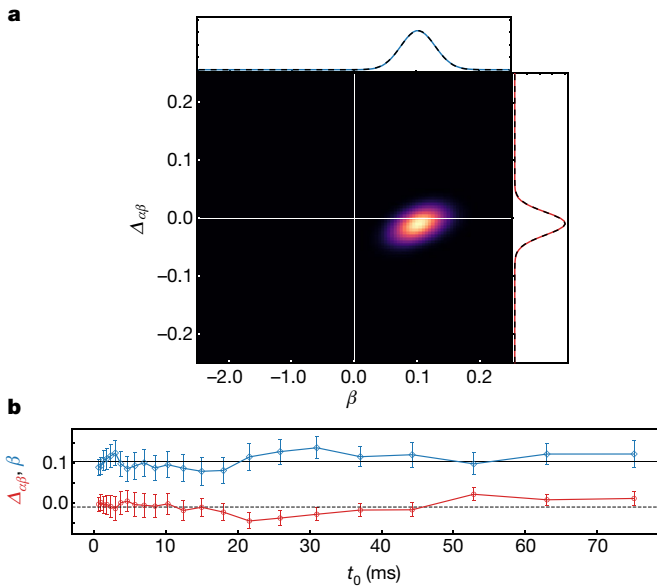


Fig. 3 | Scaling exponents. **a**, The combined two-dimensional likelihood function (colour scale), averaged over all times t and reference times t_0 within the scaling period and over three different initial conditions, reveals a clear peak that yields the non-vanishing scaling exponents $\alpha \approx \beta = 0.1 \pm 0.03$, with a deviation between the two exponents of $\Delta_{\alpha\beta} = \alpha - \beta = -0.01 \pm 0.02$. The error is estimated using a Gaussian fit (black dashed lines) to the marginal-likelihood function (top and right). **b**, Dependence of the scaling exponents on the reference time t_0 . The exponents are, to a good approximation, independent of t_0 and agree well with the mean predictions (black solid and dashed lines). The error bars denote the standard deviation obtained from a Gaussian fit to the marginal-likelihood functions at each reference time separately.

function shifts with time towards lower momentum scales while the occupancy grows in the infrared. In general, $n(k, t)$ depends on k and t separately.

However, it has been suggested⁴ that overpopulated fields far from equilibrium can give rise to universal behaviour, signalled by the infrared scaling property of the distribution function

$$n(k, t) = (t/t_0)^\alpha f_S((t/t_0)^\beta k) \quad (1)$$

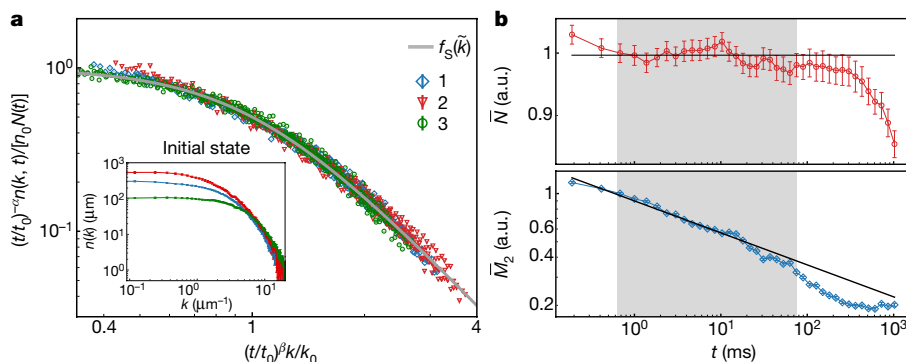


Fig. 4 | Universal scaling function and spatially averaged observables. **a**, Normalized universal scaling function for varying initial conditions: (1) blue, $N = 1,700$, $n_s = 1.4 \mu\text{m}^{-1}$; (2) red, $N = 2,800$, $n_s = 0.9 \mu\text{m}^{-1}$; (3) green, $N = 1,150$, $n_s = 2.3 \mu\text{m}^{-1}$. All initial conditions collapse to a single universal function f_S with exponent $\zeta = 2.39 \pm 0.18$ (grey solid line) for all times within the scaling region. The non-universal scales are the characteristic momentum scale, $k_0 = 2.61 \mu\text{m}^{-1}$ (blue), $2.28 \mu\text{m}^{-1}$ (red) and $3.97 \mu\text{m}^{-1}$ (green), and the global scaling factor of the momentum distribution, $n_0 = 0.14 \mu\text{m}$, $0.15 \mu\text{m}$ and $0.10 \mu\text{m}$, respectively. The rescaled experimental data are binned over three adjacent points in k for clarity. The small deviations at low momenta are due to the finite expansion time

where t_0 denotes an arbitrary reference time within the period when $n(k, t)$ exhibits the scaling behaviour.

Figure 2b demonstrates that scaling exponents α and β can indeed be found such that, in the infrared, the rescaled distributions $(t/t_0)^{-\alpha} n(\tilde{k}, t)$ as functions of the rescaled momenta $\tilde{k} = (t/t_0)^\beta k$ collapse to a single curve $f_S(\tilde{k}) = n(\tilde{k}, t_0)$. This indicates that below a characteristic momentum scale k_s , the distribution function $n(k, t)$ depends on space and time only through the scaling of a single universal function $f_S(\tilde{k})$. The scaling exponents are found to be $\alpha = 0.09 \pm 0.05$ and $\beta = 0.1 \pm 0.04$, which indicates that $\alpha \approx \beta$ (see Methods for details on the error estimation).

We demonstrate the predicted insensitivity of the universal properties to the initial state by comparing the evolution for different initial conditions before and after the cooling quench. We find excellent agreement for the scaling exponents, obtained independently by using a scaling analysis for each of the three measurements (Extended Data Figs. 2–5). This shows the generality and robustness of these non-equilibrium attractor solutions: in contrast to equilibrium critical phenomena, for which the temperature has to be adjusted to observe scaling, no fine-tuning of parameters is required.

The universal character allows us to relate the predictions for each measurement directly, resulting in the combined likelihood function presented in Fig. 3a. We consider, for the analysis, the approximately uncorrelated exponents β and $\Delta_{\alpha\beta} = \alpha - \beta$. In agreement with each individual measurement, we find a clearly non-vanishing exponent $\beta = 0.1 \pm 0.03$ and a vanishing (within errors) exponent $\Delta_{\alpha\beta} = -0.01 \pm 0.02$, and thus $\alpha = 0.09 \pm 0.03$. The expected independence of the scaling exponents α and β on the reference time t_0 is shown in Fig. 3b.

We further demonstrate that the shape of the scaling function $f_S(\tilde{k})$ in Fig. 4 is universal: the data for three different initial conditions follow a single universal function $f_S(\tilde{k})$ for all times during which the system shows scaling dynamics. This reflects an enormous reduction of the possible dependence of the dynamics on variations in time and momentum, because the scaling function depends on only the relevant parameters of the system. For instance, if an initial field amplitude represented a relevant parameter, then the scaling function would additionally depend on the product of time or momentum and this field amplitude, with a new scaling exponent. In this case, extracting the scaling function as in Fig. 2 or Fig. 4 as a function of only the product of time and momentum would fail to describe the data.

of the gas (Methods). The initial single-particle momentum distribution $n(k)$ at the end of the quench is depicted in the inset. We note the double logarithmic scale, in contrast to Fig. 2. **b**, Scaling of averaged observables. The fraction of particles in the scaling region $\tilde{N} \propto (t/t_0)^{\Delta_{\alpha\beta}}$ (upper panel) becomes approximately conserved (solid black line) within the scaling period (grey-shaded region) while being transported towards lower momenta. Deviations in the scaling of the mean kinetic energy per particle in the scaling region, $\tilde{M}_2 \propto (t/t_0)^{-2\beta}$ (lower panel), from the predicted scaling (solid black line) indicates the extent of the scaling period in time. The error bars mark the 95% confidence interval. a.u., arbitrary units.

We consider the form $f_s \propto [1 + (\tilde{k}/k_0)^\zeta]^{-1}$ for the scaling function^{4,29}, where the exponent $\zeta = 2.39 \pm 0.18$ is obtained from a single maximum-likelihood fit to all experimental realizations simultaneously. For a fixed exponent, the non-universal scales—the global scaling factor of the momentum distribution and the momentum scale k_0 that rescales the dimensionless momentum \tilde{k}/k_0 —are determined from a least-squares fit for each experimental realization (Methods). The shape of the momentum distribution within the scaling period is markedly different from the thermal distribution (compare Fig. 1c and Extended Data Fig. 1), which clearly indicates a non-thermal scaling phenomenon.

The extent of the scaling region in time is visible from the scaling behaviour of the spatially averaged observables \bar{N} and \bar{M}_2 (Methods), which describe the fraction of particles and the mean energy per particle in the time-dependent scaling region of momentum space ($|k| \leq (t/t_0)^\beta k_S$), respectively. From the scaling ansatz in equation (1), we find $\bar{N} \propto (t/t_0)^{\Delta_{\alpha\beta}}$ and hence (because $\Delta_{\alpha\beta} \approx 0$) the emergence of a conserved quantity. This is confirmed in Fig. 4b, in which \bar{N} is approximately constant in the scaling period, whereas it shows a clear time dependence before and after.

The values for the scaling exponents α and β determine the direction and speed with which the particles are being transported. Because these values are positive, a given momentum k in this regime scales as $k/k_0 \propto t^{-\beta}$, so the transport is directed towards lower momenta (the infrared). This transport of particle number leads ultimately to the observed build-up of the quasi-condensate and the approach to thermal equilibrium at late times. The mean energy also exhibits power-law behaviour, $\bar{M}_2 \propto (t/t_0)^{-2\beta}$, and is in accordance with the determined scaling exponent β . Therefore, whereas the particle number in the scaling region is conserved, energy is transported outside this region to higher momenta. On the basis of the scaling properties of these global observables, we identify the scaling period to include the times $t \approx 0.7\text{--}75$ ms.

The far-from-equilibrium universal scaling dynamics in isolated Bose gases following a strong cooling quench or for equivalent initial conditions has been studied theoretically using non-perturbative kinetic equations^{4,13}. In these studies, the universal scaling function is expected to depend on the dimensionality d . The predicted¹³ power-law fall-off $n(k) \propto k^{-\zeta}$, with $\zeta = d + 1$, is consistent with the approximate form of the scaling function given by the RDM and by the quasi-condensate at low momentum, but differs (slightly) from the experimental results. A scaling analysis of the kinetic quasiparticle transport⁴ yields the exponent $\beta = 1/2$ in equation (1) to be independent of d . However, this theory is not expected to apply fully. In particular, for $d = 1$, owing to the kinematic restrictions from energy and momentum conservation, the associated transport is expected to vanish.

The contributions of higher dimensions to the one-dimensional physics provide a plausible way of explaining the non-standard scaling function and scaling exponents observed. Initially, there is a small population of atoms with momenta large enough to excite thermalizing collisions³⁰, and a very small initial seed can lead to thermalization, as observed previously³¹. This is confirmed by a quasi-condensate fit to the final momentum distribution, which, assuming thermal equilibrium, yields an excited-state population of 11% ($T = 95$ nK = $0.6\hbar\omega_\perp$). Our experimental results provide a quantum simulation near the dimensional crossover between one- and three-dimensional physics, establishing universal scaling dynamics far from equilibrium in a regime in which no theoretical predictions are currently available.

The direct experimental evidence that we have presented of scaling dynamics in an isolated far-from-equilibrium system is a crucial step towards a description of non-equilibrium evolution by non-thermal fixed points. Similar phenomena have recently been observed³² in a spin-1 system, but with a scaling exponent of $\beta \approx 1/2$. The concept of non-thermal fixed points has the potential to provide a unified description of non-equilibrium evolution, reminiscent of the characterization of equilibrium critical phenomena in terms of renormalization-group fixed points³³. Such a description may lead to a comprehensive

classification of systems on the basis of their universal properties far from equilibrium, which would be relevant for a large variety of systems at different scales.

Online content

Any methods, additional references, Nature Research reporting summaries, source data, statements of data availability and associated accession codes are available at <https://doi.org/10.1038/s41586-018-0667-0>.

Received: 30 May; Accepted: 28 September 2018;

Published online 7 November 2018.

- Polkovnikov, A., Sengupta, K., Silva, A. & Vengalattore, M. Colloquium: Nonequilibrium dynamics of closed interacting quantum systems. *Rev. Mod. Phys.* **83**, 863–883 (2011).
- Gogolin, C. & Eisert, J. Equilibration, thermalisation, and the emergence of statistical mechanics in closed quantum systems. *Rep. Prog. Phys.* **79**, 056001 (2016).
- Berges, J., Rothkopf, A. & Schmidt, J. Nonthermal fixed points: effective weak coupling for strongly correlated systems far from equilibrium. *Phys. Rev. Lett.* **101**, 041603 (2008).
- Piñeiro Orioli, A., Boguslavski, K. & Berges, J. Universal self-similar dynamics of relativistic and nonrelativistic field theories near nonthermal fixed points. *Phys. Rev. D* **92**, 025041 (2015).
- Micha, R. & Tkachev, I. I. Relativistic turbulence: a long way from preheating to equilibrium. *Phys. Rev. Lett.* **90**, 121301 (2003).
- Moore, G. D. Condensates in relativistic scalar theories. *Phys. Rev. D* **93**, 065043 (2016).
- Berges, J., Boguslavski, K., Schlichting, S. & Venugopalan, R. Universality far from equilibrium: from superfluid Bose gases to heavy-ion collisions. *Phys. Rev. Lett.* **114**, 061601 (2015).
- Baier, R., Mueller, A. H., Schiff, D. & Son, D. T. “Bottom-up” thermalization in heavy ion collisions. *Phys. Lett. B* **502**, 51–58 (2001).
- Berges, J., Boguslavski, K., Schlichting, S. & Venugopalan, R. Turbulent thermalization process in heavy-ion collisions at ultrarelativistic energies. *Phys. Rev. D* **89**, 074011 (2014).
- Scholle, J., Nowak, B. & Gasenzer, T. Critical dynamics of a two-dimensional superfluid near a nonthermal fixed point. *Phys. Rev. A* **86**, 013624 (2012).
- Svistunov, B. V. Highly nonequilibrium Bose condensation in a weakly interacting gas. *J. Moscow Phys. Soc.* **1**, 373–390 (1991).
- Schmidt, M., Erne, S., Nowak, B., Sexty, D. & Gasenzer, T. Non-thermal fixed points and solitons in a one-dimensional Bose gas. *New J. Phys.* **14**, 075005 (2012).
- Chantesana, I., Piñeiro Orioli, A. & Gasenzer, T. Kinetic theory of non-thermal fixed points in a Bose gas. Preprint at <https://arxiv.org/abs/1801.09490> (2018).
- Deng, J., Schlichting, S., Venugopalan, R. & Wang, Q. Off-equilibrium infrared structure of self-interacting scalar fields: universal scaling, vortex-antivortex superfluid dynamics, and Bose-Einstein condensation. *Phys. Rev. A* **97**, 053606 (2018).
- Hohenberg, P. C. & Halperin, B. I. Theory of dynamic critical phenomena. *Rev. Mod. Phys.* **49**, 435–479 (1977).
- Kolmogorov, A. N. The local structure of turbulence in incompressible viscous fluid for very large Reynolds numbers. *Dokl. Akad. Nauk SSSR* **30**, 299–303 (1941).
- Sieberer, L. M., Huber, S. D., Altman, E. & Diehl, S. Dynamical critical phenomena in driven-dissipative systems. *Phys. Rev. Lett.* **110**, 195301 (2013).
- Navon, N. et al. Synthetic dissipation and cascade fluxes in a turbulent quantum gas. Preprint at <https://arxiv.org/abs/1807.07564> (2018).
- del Campo, A. & Zurek, W. H. Universality of phase transition dynamics: Topological defects from symmetry breaking. *Int. J. Mod. Phys. A* **29**, 1430018 (2014).
- Navon, N., Gaunt, A. L., Smith, R. P. & Hadzibabic, Z. Critical dynamics of spontaneous symmetry breaking in a homogeneous Bose gas. *Science* **347**, 167–170 (2015).
- Clark, L. W., Feng, L. & Chin, C. Universal space-time scaling symmetry in the dynamics of bosons across a quantum phase transition. *Science* **354**, 606–610 (2016).
- Bray, A. J. Theory of phase-ordering kinetics. *Adv. Phys.* **43**, 357–459 (1994).
- Calabrese, P. & Gambassi, A. Ageing properties of critical systems. *J. Phys. A* **38**, R133–R139 (2005).
- Berges, J., Borsányi, S. & Wetterich, C. Prethermalization. *Phys. Rev. Lett.* **93**, 142002 (2004).
- Gring, M. et al. Relaxation and prethermalization in an isolated quantum system. *Science* **337**, 1318–1322 (2012).
- Chiocchetta, A., Gambassi, A., Diehl, S. & Marino, J. Dynamical crossovers in prethermal critical states. *Phys. Rev. Lett.* **118**, 135701 (2017).
- Smith, D. A. et al. Absorption imaging of ultracold atoms on atom chips. *Opt. Express* **19**, 8471–8485 (2011).
- Bücker, R. et al. Single-particle-sensitive imaging of freely propagating ultracold atoms. *New J. Phys.* **11**, 103039 (2009).
- Karl, M. & Gasenzer, T. Strongly anomalous non-thermal fixed point in a quenched two-dimensional Bose gas. *New J. Phys.* **19**, 093014 (2017).
- Mazets, I. E., Schumm, T. & Schmiedmayer, J. Breakdown of integrability in a quasi-1D ultracold Bosonic gas. *Phys. Rev. Lett.* **100**, 210403 (2008).

31. Li, C. et al. Dephasing and relaxation of bosons in 1D: Newton's cradle revisited. Preprint at <https://arxiv.org/abs/1804.01969> (2018).
32. Prüfer, M. et al. Observation of universal quantum dynamics far from equilibrium. *Nature* <https://doi.org/10.1038/s41586-018-0659-0> (2018).
33. Wilson, K. G. The renormalization group: critical phenomena and the Kondo problem. *Rev. Mod. Phys.* **47**, 773–840 (1975).

Acknowledgements We thank J. Brand, L. Carr, M. Karl, P. Kevrekidis, P. Kunkel, D. Linnemann, A. N. Mikheev, B. Nowak, M. K. Oberthaler, J. M. Pawłowski, A. Piñeiro Orioli, M. Prüfer, W. Rohringer, C. M. Schmied, M. Schmidt, J. Schole and H. Strobel for discussions. We thank T. Berrada, S. van Frank, J.-F. Schaff and T. Schumm for help with the experiment during data collection. This work was supported by the SFB 1225 'ISOQUANT' and grant number GA677/7,8 financed by the German Research Foundation (DFG) and Austrian Science Fund (FWF), the ERC advanced grant QuantumRelax, the Helmholtz Association (HA216/EMMI), the EU (FET-Proactive grant AQuS, project number 640800) and Heidelberg University (CQD). S.E. acknowledges partial support through the EPSRC project grant (EP/P00637X/1). J.S., J.B. and T.G. acknowledge the hospitality of the Erwin Schrödinger Institut in the framework of their thematic programme 'Quantum Paths'.

Reviewer information *Nature* thanks M. Kolodrubetz and the other anonymous reviewer(s) for their contribution to the peer review of this work.

Author contributions S.E. performed the analysis, adapted the theory and wrote the paper, J.S. designed the experiment; R.B. conducted the experiment and initial data analysis. All authors contributed to interpreting the data and writing the manuscript.

Competing interests The authors declare no competing interests.

Additional information

Extended data is available for this paper at <https://doi.org/10.1038/s41586-018-0667-0>.

Reprints and permissions information is available at <http://www.nature.com/reprints>.

Correspondence and requests for materials should be addressed to J.S.

Publisher's note: Springer Nature remains neutral with regard to jurisdictional claims in published maps and institutional affiliations.

METHODS

Preparation of the gas and cooling quench. The initial thermal Bose gas is prepared using a standard procedure to produce ultracold gases of ^{87}Rb on an atom chip³⁴. The description of the system at the microscale is given by the Bose Hamiltonian with contact interactions, determined by the s -wave scattering length $a_s = 5.2$ nm. We prepare a thermal cloud of typically $N = (2.7\text{--}3.2) \times 10^4$ atoms initially in an elongated, $\omega_{\parallel} = 2\pi \times 23$ Hz and $\omega_{\perp} = 2\pi \times 3.3$ kHz, deep trapping potential $V_i \approx h \times (130\text{--}160)$ kHz at a temperature $T \approx 530\text{--}600$ nK. The atoms are held in this configuration for 100 ms to ensure a well defined initial state. The thermal cloud is above both the dimensional crossover to an effective one-dimensional system and the critical temperature T_c for the phase transition to a three-dimensional Bose–Einstein condensate, and therefore has a large excess of particles in transversally excited, high-energy states. The trap depth is reduced to its final value V_f at a constant rate $R_q = (V_i - V_f)/\tau_q = h \times 25$ kHz ms^{-1} by applying radio-frequency radiation at a time-dependent frequency (RF-knife), leading to an energy-dependent transition of atoms from a trapped to an un-trapped spin state. This allows the high-energy particles to rapidly leave the trap, leading to the competing timescales τ_q of the cooling quench (see Fig. 1) and the typical collision times needed for re-equilibration of the system. The final trap depth is $V_f \approx h \times 2$ kHz, which is below the first radially excited state of the trapping potential, $hV_f < h\omega_{\perp}$. At the end of the cooling ramp, the RF-knife is held at its final position for 0.5 ms before it is faded out within 1 ms, thereby raising the trap depth to $V \approx h \times 20$ kHz. In addition, because the RF-knife reduces the radial trapping frequency slightly, there is a small interaction quench (about 10%) of the one-dimensional system. The system is therefore rapidly quenched to the quasi-one-dimensional regime, finally occupying only the transverse ground state. Experimental realizations 1 to 3 reported in the main text have final atom numbers of $N \approx 1,700, 2,800$ and $1,150$, respectively, and agree well with the RDM with a defect density of $n_s = 1.4 \mu\text{m}^{-1}, 0.9 \mu\text{m}^{-1}$ or $2.3 \mu\text{m}^{-1}$ and defect width of $\xi_s = 0.07 \mu\text{m}, 0.06 \mu\text{m}$ or $0.05 \mu\text{m}$ (corresponding to $\xi_s/\xi_h = 0.3, 0.3$ or 0.17). The resultant far-from-equilibrium state is held for variables times of up to $t \approx 1$ s, during which the universal dynamics develops and takes place.

Measuring the density and momentum distributions. The density and momentum distribution of the gas are measured after finite time of flight for $t_{\text{tof}} = 1.5$ ms and $t_{\text{tof}} = 46$ ms of free expansion. This gives access to the in situ (IS) and time-of-flight (tof) density profiles, for which the atoms are detected using absorption and fluorescent imaging in a thin light sheet, respectively. We then calculate the radially centred and integrated density profiles in the longitudinal direction. We correct the profiles for possible random sloshing effects. The quench and measurement is repeated for each experimental shot and hold time t , 10–15 times for the in situ data and 25–50 times for the time-of-flight data. The fast expansion in the radial direction dilutes the gas and leads to ballistic expansion in the longitudinal direction. Because the momentum of the particles during the expansion is therefore approximately conserved, the density distribution after expansion converges to the in situ momentum distribution of the cloud. We checked the effects of a finite dilution time via numerical simulations of the Gross–Pitaevskii equation, using hydrodynamic models to determine the time dependence of the interaction constant g for early times of the expansion. For the parameters of the experiment, we did not find any substantial deviations from a completely ballistic expansion in the longitudinal direction.

The pulled-back momentum distribution converges rapidly for high k towards the true momentum distribution of the gas. For low k the finite in situ size of the cloud does not allow for a clear separation of different momentum modes and atoms of different momentum overlap in the measured density after time of flight. This means that for a cloud of size R , particles with momentum less than about $k_{\text{IS}} = Rm/(\hbar t_{\text{tof}})$ do not have time to propagate sufficiently far outside the in situ bulk density to be clearly separated. Therefore, the pulled-back momentum distribution for $k \lesssim k_{\text{IS}}$ resembles the in situ density profile rather than the actual momentum distribution of the gas.

Scaling analysis. We extract the universal scaling exponents α and β using a least-squares fit of the analytical prediction in equation (1), minimizing

$$\chi^2(\alpha, \beta) = \frac{1}{N_t^2} \sum_{t, t_0} \chi_{\alpha, \beta}^2(t, t_0) \quad (2)$$

where we average over all times t and reference times t_0 within the scaling period. The local $\chi_{\alpha, \beta}^2(t, t_0)$ is calculated via

$$\chi_{\alpha, \beta}^2(t, t_0) = \int_{k_1}^{k_h} \frac{[(t/t_0)^{\alpha} \bar{n}((t/t_0)^{\beta} k, t_0) - \bar{n}(k, t)]^2}{\bar{\sigma}((t/t_0)^{\beta} k, t_0)^2 + \bar{\sigma}(k, t)^2} dk$$

where σ denotes the standard error of the mean, and $\bar{n}(k, t) = n(k, t)/N(t)$ and $\bar{\sigma}(k, t) = \sigma(k, t)/N(t)$ are normalized by the total atom number to minimize the influence of atom loss during the evolution; however, the atom loss is negligible

during the time period when the system shows scaling behaviour. For later times the atom loss is roughly 10% per 100 ms, with a final atom number of approximately 40% at the end of the evolution. The rescaling of the momentum variable inevitably necessitates a comparison between the momentum distributions at momenta lying between the discrete values measured in the experiment. We therefore linearly interpolate the spectrum and its error at the reference time t_0 , which allows us to evaluate the experimental spectrum at all momenta $(t/t_0)^{\beta} k$. For the scaling analysis we symmetrize the spectrum by averaging the momentum distribution over $\pm k$ to lower the noise level.

Estimating the exponents and their error is done via the likelihood function. To decouple the two exponents we take $\alpha = \beta + \Delta_{\alpha, \beta}$ and fit the deviation $\Delta_{\alpha, \beta}$ of the exponent from the theoretical expectation $\alpha \equiv \beta$. We therefore define the likelihood function

$$L(\Delta_{\alpha, \beta}, \beta) = \exp\left[-\frac{1}{2} \chi^2(\Delta_{\alpha, \beta}, \beta)\right] \quad (3)$$

The most probable exponents are determined by the maximum of the likelihood function. The error of the estimate is determined by integrating the two-dimensional likelihood function along one dimension and extracting the variance of the remaining exponent using a Gaussian fit to the marginal-likelihood functions. We find excellent agreement between the marginal likelihood functions and the Gaussian fits. Therefore, the Gaussian estimate of the error is equivalent to the (asymmetric) estimate using a change in the log-likelihood function by 1/2. The reason for this good agreement is the aforementioned decoupling of the exponent, which results to a good degree in a two-dimensional, Gaussian likelihood function for $L(\Delta_{\alpha, \beta}, \beta)$. The estimates of the scaling exponents for different reference times are calculated equivalently (neglecting the sum over t_0 in equation (2)). The estimate is insensitive to the upper cut-off k_h (within reasonable limits). The momentum k_S , which limits the scaling region in the ultraviolet, is determined as the characteristic scale for which the mean deviation of the rescaled momentum distributions for $|k| \leq k_S$ and averaged over all times t in the scaling period exceeds the 95% confidence interval at the reference time t_0 . The lower cut-off is taken as $k_l = 0$. Excluding momenta $|k| \leq k_S$ leads to a small shift in the exponents towards lower values, but agrees well within the estimated errors of the exponents (less than about 0.3σ deviation). The results of the scaling analysis for three independent experimental realizations are shown in Extended Data Figs. 2–4. We find similar results in all cases. The exponents and errors reported in the main text are estimated from the combined likelihood function $L = \prod_i L_i$, where i labels the independent experimental realizations.

The universal function f_S is determined equivalently, where for each fixed exponent ζ the non-universal scales are determined from a least-squares fit to each experimental realization separately. To minimize the influence of the finite expansion of the gas, we consider momenta $|k| > k_{\text{IS}}$ for the determination of f_S . The likelihood function is subsequently defined by the averaged residuals of the scaled data as compared to the universal scaling function $f_S = (1 + k^{\zeta})^{-1}$ for all realizations simultaneously. The error is again estimated using a Gaussian fit to the (one-dimensional) likelihood function. The non-universal scales for the most likely exponent $\zeta = 2.39 \pm 0.18$ for experimental realizations 1 to 3 are the characteristic momentum scale, $k_0 = 2.61 \mu\text{m}^{-1}, 2.28 \mu\text{m}^{-1}$ and $3.97 \mu\text{m}^{-1}$, respectively, and the global scaling factor of the momentum distribution, $n_0 = 0.14 \mu\text{m}, 0.15 \mu\text{m}$ and $0.10 \mu\text{m}$.

Global observables. We define the global observables

$$\bar{N} = \int_{|k| \leq (t/t_0)^{-\beta} k_S} \frac{n(k, t)}{N(t)} dk \propto (t/t_0)^{-\Delta_{\alpha, \beta}} \quad (4)$$

$$\bar{M}_{n \geq 1} = \int_{|k| \leq (t/t_0)^{-\beta} k_S} \frac{|k|^n n(k, t)}{N\bar{N}(t)} dk \propto (t/t_0)^{-n\beta} \quad (5)$$

where $k_S = 6.5\text{--}8 \mu\text{m}^{-1}$ defines the high-momentum cut-off for the scaling region in k . In the main text, we consider the fraction of particles in the scaling region $\bar{N} \propto (t/t_0)^{\Delta_{\alpha, \beta}}$ and the mean kinetic energy per particle in the scaling region $\bar{M}_2 \sim (t/t_0)^{-2\beta}$. The global observables \bar{N} and \bar{M} show independent scaling in time with the exponents $\Delta_{\alpha, \beta}$ and β , whereas the integral ranges depend non-trivially on β . The results for each experimental realization are shown in Extended Data Fig. 5. In the main text, we report the result obtained by averaging over all experimental realizations. **Model fits.** The density profile $\rho(z)$ is determined by a fit to the experimental in situ density, measured after $t_{\text{tof}} = 1.5$ ms of free expansion. In case of the RDM we consider for a fixed atom number $N(t)$ and a scaled density profile $\rho(z, t) = b^{-1}(t)\rho(zb^{-1}(t))$ in the Thomas–Fermi approximation, leaving the scaling factor $b(t)$ as the only free parameter (more precisely, a previous result³⁵ is used for the density profile, which takes the radial swelling of the condensate into account). We neglect possible finite-temperature fluctuations and any contributions

from radially excited states in the RDM, assuming the gas to be dominated by solitonic defects. For early times, the high-momentum modes do not have substantial thermal occupation, and we find good accordance with the RDM.

In case of the quasi-condensate, we determine the thermal density profile for a given temperature T and chemical potential μ using simulations of the stochastic Gross–Pitaevskii equation (see, for example, ref. ³⁶). The broadening of the density distribution is herein due to the finite temperature of the gas. The density profile is subsequently fitted via $\rho(z, t) = \rho_{\text{QC}}(z, T(t), \mu(t)) + \rho_{\perp}(z, T(t), \mu(t))$. Here we take into account the thermal occupation of radially excited states ρ_{\perp} within the semiclassical approximation, which are non-negligible for late times. The chemical potential μ is fixed by the total atom number, $\int \rho(z, t) dz = N(t)$.

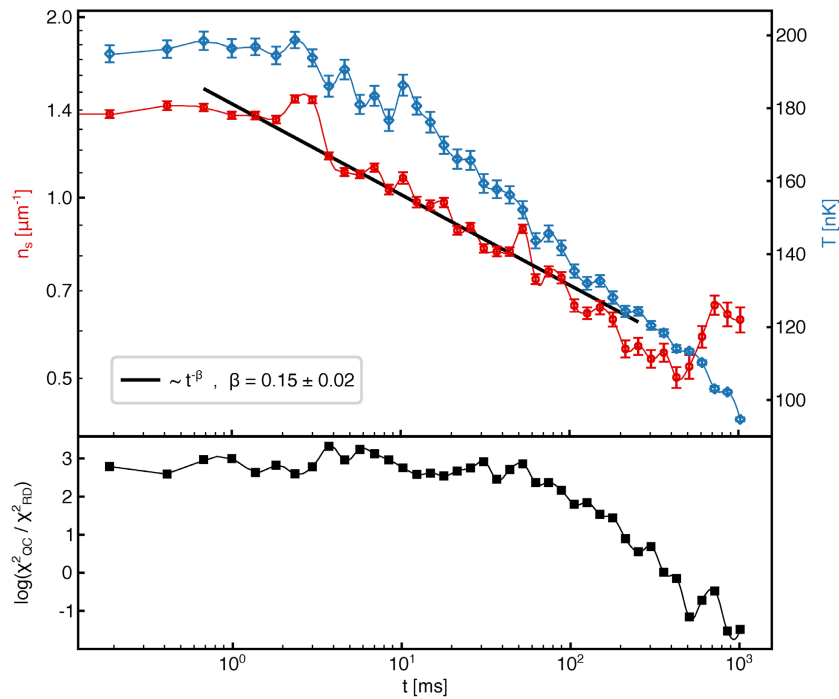
The fitted density profiles are used to determine the single-particle momentum distribution $n(k, t)$ of the inhomogeneous system from a least-squares fit of the experimental data to the theoretical predictions within the local density approximation. For both models we restrict the fitting region to $|k| > k_{\text{is}}$, owing to the simplified hydrodynamic model for the finite expansion of the gas. The RDM¹² is fitted over the full momentum range that is accessible in the experiment. For high defect densities, the RDM fit shows correlations between defect density and width because these two scales become of the same order for the far-from-equilibrium state. Because it is theoretically expected that the defect width is approximately conserved during evolution, we fix the defect width to its mean value within the first 25 ms of evolution, leaving the defect density as the only free parameter. We find reasonable agreement between the RDM results and the independent scaling analysis. In particular, the RDM is clearly preferred compared to a thermal distribution within the scaling period.

For the fits in thermal equilibrium we consider a quasi-condensate model³⁷, including thermal occupation of radially excited states³⁸. Considering the validity regime of the quasi-condensate model, we restrict the fitting procedure to momentum modes with energy less than $\hbar\omega_{\perp}$. We determine the chemical potential μ by fixing the atom number within this region of momentum space. This leads to a slight shift in the chemical potential compared to the in situ fits. For late times we find excellent agreement with the experimental data, demonstrating the relaxation of the system to thermal equilibrium.

Data availability

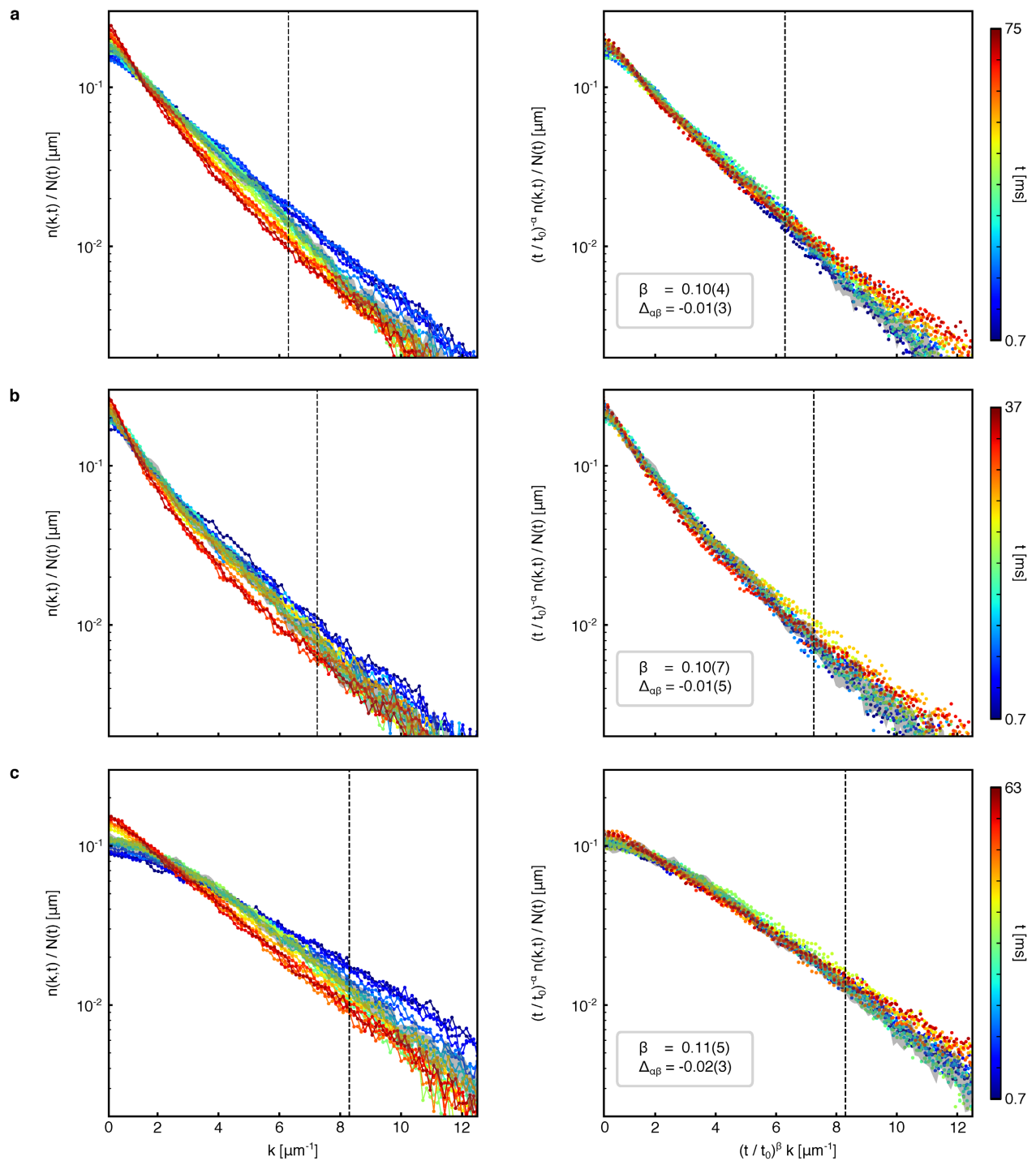
The data that support the findings of this study are available from the corresponding author on reasonable request.

34. Reichel, J. & Vuletic, V. *Atom chips* (John Wiley & Sons, Weinheim, 2011).
35. Gerbier, F. Quasi-1D Bose–Einstein condensates in the dimensional crossover regime. *Europhys. Lett.* **66**, 771–777 (2004).
36. Blakie, P. B., Bradley, A. S., Davis, M. J., Ballagh, R. J. & Gardiner, C. W. Dynamics and statistical mechanics of ultra-cold Bose gases using c-field techniques. *Adv. Phys.* **57**, 363–455 (2008).
37. Richard, S. et al. Momentum spectroscopy of 1D phase fluctuations in Bose–Einstein condensates. *Phys. Rev. Lett.* **91**, 010405 (2003).
38. Davis, M. J., Blakie, P. B., van Amerongen, A. H., van Druten, N. J. & Kheruntsyan, K. V. Yang–Yang thermometry and momentum distribution of a trapped one-dimensional Bose gas. *Phys. Rev. A* **85**, 031604 (2012).



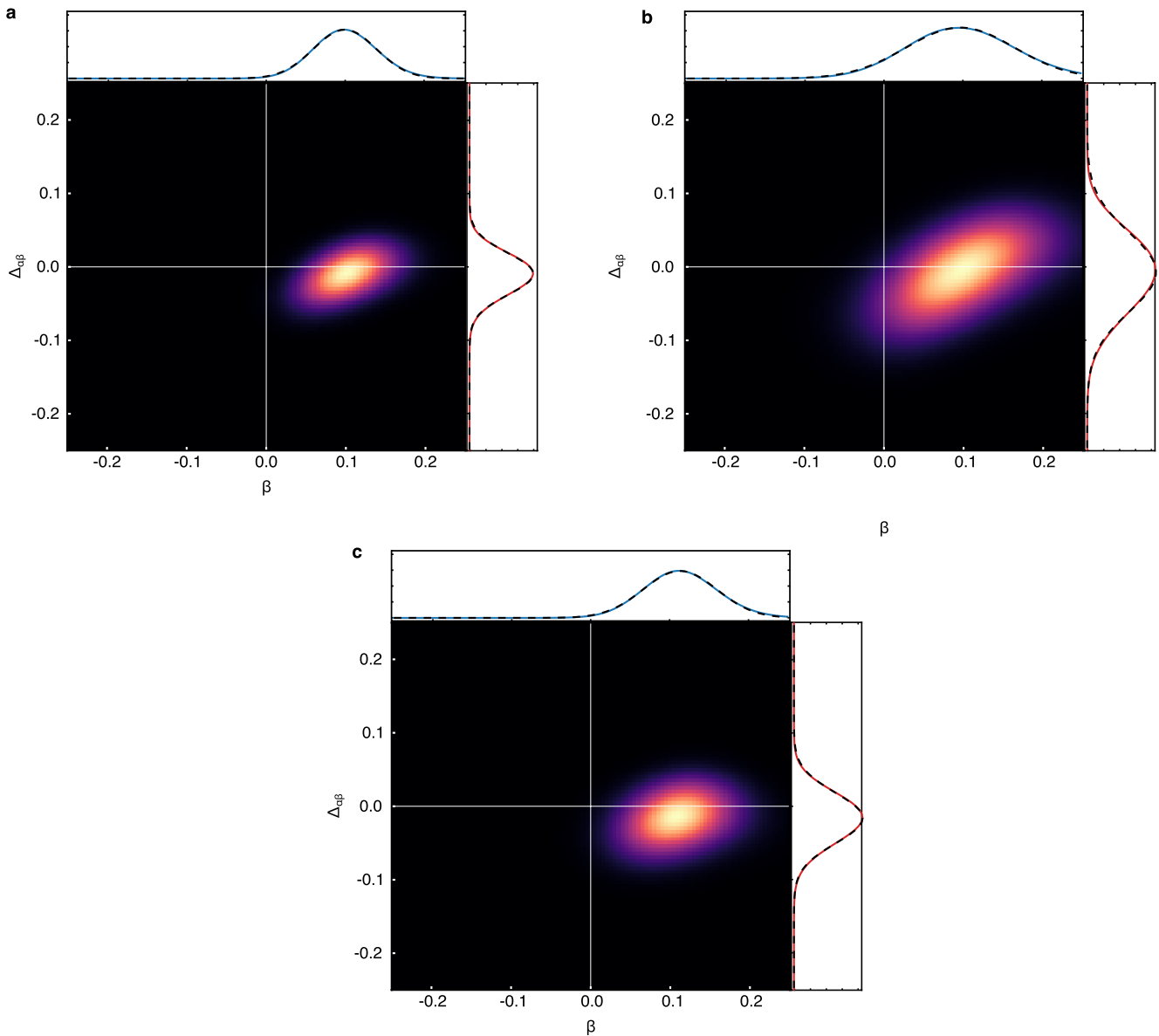
Extended Data Fig. 1 | Results of random-defect and quasi-condensate models. The time evolution of the characteristic scales for the experimental data presented in Fig. 4a (initial condition 1) are shown. The resulting temperature T (blue) and defect density n_s (red) are shown in the upper panel for the full time evolution. The defect width for the random-defect model is fixed to $\xi_s = 0.087 \mu\text{m}$, determined by the mean over the first 25 ms of the evolution. The defect density within the scaling region shows a power-law dependence consistent with the exponent β of the scaling evolution reported in the main text. For later times deviations

occur, signalling the end of the scaling region. The quality of the model fit is depicted in the lower panel (black squares), where positive and negative values favour the random-defect and quasi-condensate models, respectively. The random-defect model is strongly preferred for the first roughly 100 ms, after which the system converges to a thermal quasi-condensate within about 400 ms. The absolute values of the reduced χ^2 for the random-defect (RD) model are about 1 and 5 for early and late times, respectively; those for the quasi-condensate (QC) model are about 25 and 1.



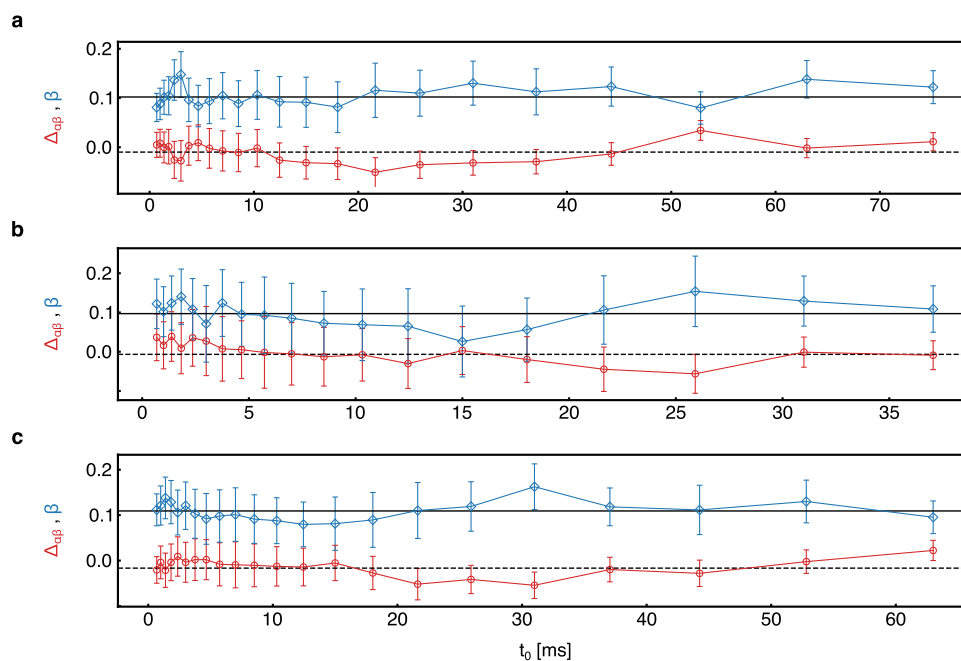
Extended Data Fig. 2 | Rescaling analysis for different initial conditions. a–c, Original (left) and rescaled (right) single-particle momentum distribution $n(k, t)$ for different initial conditions (a–c correspond to initial conditions 1–3 in Fig. 4a). Each distribution is normalized by the time-dependent atom number $N(t)$ and the time is encoded in the colour scale. The grey dashed vertical lines indicate

the scaling regime in k . The scaling exponents $\alpha \approx \beta$ and the deviation between them $\Delta_{\alpha\beta} = \alpha - \beta$ are in excellent agreement with the mean values reported in the main text. We note that here we compare the data for the full experimental resolution in k . The distribution at the reference time $t_0 = 4.7$ ms is given by the grey line; its width indicates the 95% confidence interval.



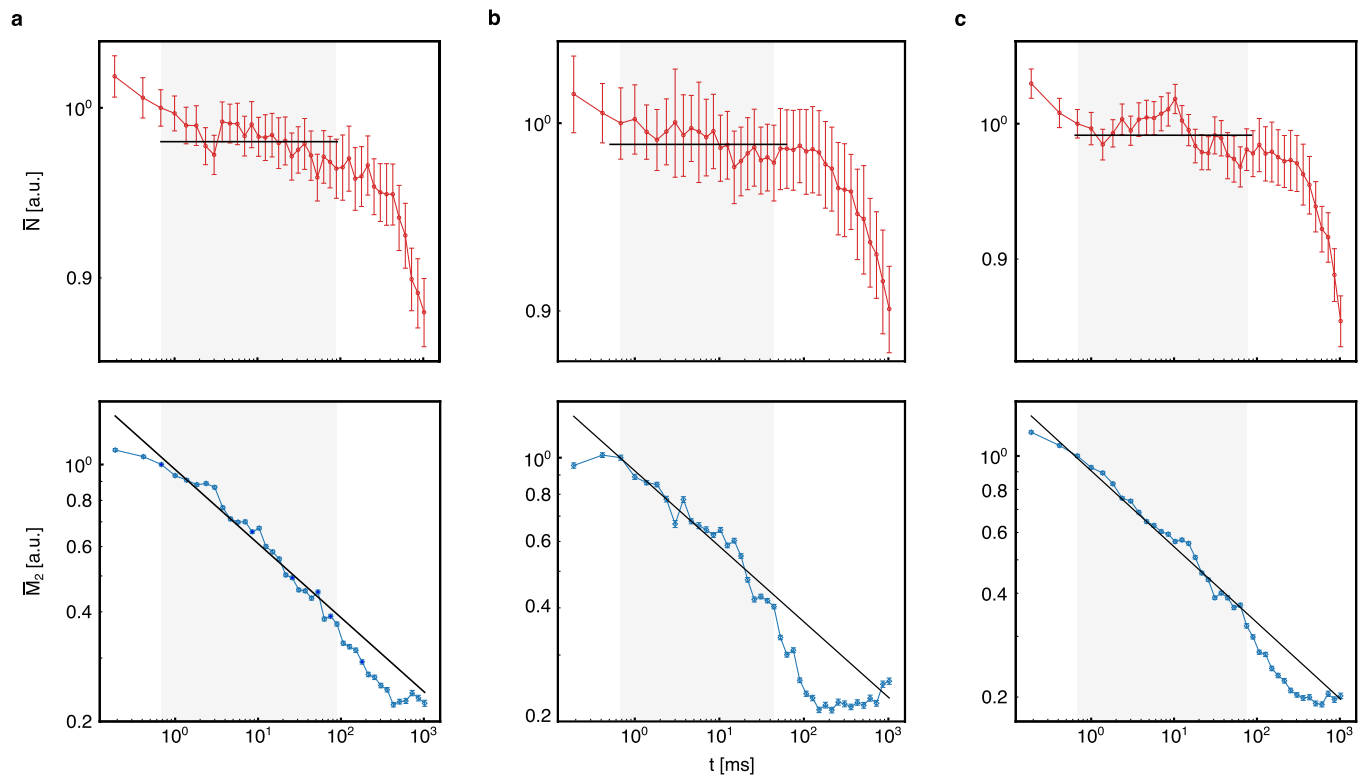
Extended Data Fig. 3 | Likelihood function for different initial conditions. **a–c**, Two-dimensional likelihood functions (colour scales) and marginal-likelihood functions (top and right) for different initial conditions (**a–c** correspond to initial conditions 1–3 in Fig. 4a). A clear peak at non-zero $\alpha \approx \beta$ is visible for each realization, whereas the deviation

between the two exponents is $\Delta_{\alpha\beta} = \alpha - \beta \approx 0$. For scan 2 (**b**), a small condensate may have been present before the quench, which led to the larger extent of the likelihood function. Gaussian fits are in excellent agreement with the marginal-likelihood functions and determine the error of the scaling exponents reported in Extended Data Fig. 2.



Extended Data Fig. 4 | Time evolution of scaling exponents for different initial conditions. **a–c**, Scaling exponents $\alpha \approx \beta$ (blue) and deviation between the two exponents $\Delta_{\alpha,\beta} = \alpha - \beta$ (red) for different initial conditions (**a–c** correspond to initial conditions 1–3 in Fig. 4a),

determined from the likelihood function for each reference time t_0 , are in good agreement with the predicted mean (black solid and dashed lines). The error bars denote the standard deviation obtained from a Gaussian fit to the marginal-likelihood function at each reference time separately.



Extended Data Fig. 5 | Spatially averaged observables for different initial conditions. **a–c**, Time evolution of the fraction of particles in the scaling region $\bar{N} \propto (t/t_0)^{\Delta_{\alpha\beta}}$ (red) and the mean kinetic energy per particle in the scaling region $\bar{M}_2 \propto (t/t_0)^{-2\beta}$ (blue) for different initial conditions

(**a–c** correspond to initial conditions 1–3 in Fig. 4a). Within the scaling region (grey-shaded areas), \bar{N} is approximately conserved. The solid black lines are the approximately conserved value and scaling solutions (5). The error bars indicate the 95% confidence interval.